DOI: https://doi.org/10.2138/am-2021-7614. http://www.minsocam.org/

AM 7614R Revision 1
A quantitative description of fission-track etching in apatite

CAROLIN ASLANIAN[1], RAYMOND JONCKHEERE[1,*], BASTIAN WAUSCHKUHN[1], AND LOTHAR RATSCHBACHER[1]

[1]Geologie, TU Bergakademie Freiberg, Bernhard-von-Cotta-Straße 2, 09599 Freiberg, Germany

ABSTRACT

We measured the apatite etch rate v_R in 5.5 M HNO_3 at 21 °C as a function of orientation. Results for Durango apatite evidence that v_R varies by a factor >5 with angle to the ***c***-axis. Our measurements also provided track etch rates v_T and surface etch rates v_S. However, these cannot be combined for calculating track etching or counting efficiencies. By inserting the measured etch rates in a recent model, we calculate the geometries and dimensions of surface tracks in different apatite faces. The proposed model must be recalibrated for different etching protocols and adapted for other minerals. We submit that the new model justifies reviewing track counting efficiencies based on the existing (v_B-v_T) etch model. We anticipate that this will have an effect on practical aspects of fission track dating. Single-track step-etch data show that the confined track lengths increase with etch time at a decreasing average rate v_L that differs from the track etch rate v_T and the apatite etch rate v_R. Both v_T and v_L exhibit large track-to-track differences that produce irreducible length variation related to the latent-track structure resulting from formation and annealing. Step etching and track width measurements are effective for reducing or eliminating procedure-related artifacts from track length data, and so for accessing more fundamental track properties.

Keywords: Apatite, fission track, etching, apatite etch rate, track etch rate.

*Email: Raymond.Jonckheere@geo.tu-freiberg.de

INTRODUCTION

Fission-track dating is based on counting the damage trails from uranium fission in natural minerals. Fission tracks are ~20 μm long in apatite (Jonckheere 2003) and ~10 nm in diameter (Paul and Fitzgerald 1992; Li et al. 2011, 2012, 2014), and too small to be seen with an optical microscope. To count them, the apatite grains are mounted, polished, and etched. This erodes the track cores, creating ~1 μm wide channels along the track axes. For accurate dating, it is important to understand the relationship between the counted number of etch channels ρ_E and the number of unetched tracks ρ_L intersecting a unit surface area. The existing track etch model describes their development as resulting from two etch rates (Price and Walker 1962; Price and Fleischer 1971; Tagami and O'Sullivan 2005; Hurford 2019). The track etch rate v_T along the track axis is the rate at which the damaged material in the track core is removed. The bulk etch rate v_B is the rate at which the surrounding material is etched in all other directions. This model implies that the etching efficiency η_E is a function of v_B and v_T; in its simplest form (Supplement 1 summarizes the variables used):

$$\eta_E = 1 - \left(\frac{v_B}{v_T}\right)^2 \qquad (1)$$

This model was developed for isotropic materials such as glasses and plastics but its application to crystalline materials was not worked out in detail. For minerals, with anisotropic v_B, equation (1) is considered to hold for the v_B value perpendicular to the etched surface. Often, η_E is taken to be the fraction of tracks counted (Hasebe et al. 2004; Tagami and O'Sullivan 2005). Equation (1) is the basis for counting tracks in slow-etching surfaces characterized by sharp polishing scratches, e.g., apatite prism faces (Gleadow 1978; 1981; Kohn et al. 2019). Mica cleavage planes are also thought to have near-unit efficiencies.

Understanding the etching process has to be fundamental to fission-track dating since it connects the channels counted and measured with a microscope to the lattice damage from uranium fission. Track etching has however received scant attention since the studies of Price and Walker (1962), Price and Fleischer (1971), and Fleischer et al. (1975). Jonckheere and Van den haute (1999) and Tagami and O'Sullivan (2005) made minor changes to equation (1) to account for tracks added as well as lost due to surface etching. Modern accounts of fission-track dating either present an etch model consistent with equation (1) (Tagami and O'Sullivan 2005; Hurford 2019; Guo et al. 2020), or a guarded description of track shapes (Gleadow et al. 2002; Donelick et al. 2005; Gleadow and Seiler 2015). This apparent consensus owes more to the lack of alternative than to actual support for the model.

Equation (1) implies that etching is efficient: $\eta_E \geqslant 0.99$ for $v_B/v_T \leqslant 0.10$; the latter value corresponds to a cone angle ($\theta = 2\arctan(v_B/v_T)$) of >10°, at least twice the average of tracks in apatite. Equation (1) also implies that η_E is independent of whether the tracks are etched in an external or internal mineral surface or an external detector. It further implies that η_E is independent of the length (distribution) of the tracks. These advantageous properties for practical fission-track dating are however not supported by evidence. Jonckheere et al. (2019) argued that the existing etch model cannot account for the dual structure of etched surface tracks, consisting of an etch pit and a track channel, e.g., in an apatite basal face, nor for the variable track shapes in different apatite faces. Measured counting efficiencies are much lower than predicted, and different for an internal surface, external surface, and external detector (Jonckheere 2003; Enkelmann et al. 2005; Jonckheere et al. 2015).

We observed that the present track-etch model is not consistent with mainstream theories of crystal growth and dissolution, and proposed a model that is (Jonckheere et al. 2019). The main difference is that the bulk etch rate v_B, the etch rate of a point on a surface, is replaced by the radial etch rate v_R of a lattice plane as a whole, i.e., its rate of displacement parallel to itself. This concept is copied from the theories of Burton et al. (1951), Frank (1958) and, among others, Irving (1959), Frank and Ives, (1960) and Jaccodine (1962), which are the basis of modern applications of crystal etching (Woensdrecht 1993; Rakovan 2002; Chernov 2004; Woodruff 2015). On the assumption that the orientations of the apatite basal and prism faces correspond to cusp-like minima in a polar etch rate plot, the proposed model accounts for the default dual structure of etched tracks and for the variation of track shapes with the orientation of the etched surface (Jonckheere et al. 2019). This contribution reports measurements of the radial etch rates v_R of apatite etched in 5.5 M HNO_3 at 21 °C. Inserting the measured rates in the proposed etch model allows us to predict not just the shape but also the dimensions of a fission track with a specified orientation intersecting a given surface.

This is the peer-reviewed, final accepted version for American Mineralogist, published by the Mineralogical Society of America.
The published version is subject to change. Cite as Authors (Year) Title. American Mineralogist, in press.
DOI: https://doi.org/10.2138/am-2021-7614. http://www.minsocam.org/

EXPERIMENT

Earlier investigations of the morphological evolution of single crystals during growth and dissolution proceeded by etching multi-facetted initial forms and observing the developing faces. Fast-etching faces grow at the expense of slow-etching faces on convex forms (polished spheres or cylinders) while the opposite is true for concave forms (hemispherical hollows or cylindrical grooves; Batterman 1957; Irving 1959; 1960; Holmes 1959; Frank and Ives 1960; Jaccodine 1962; Heimann 1971; Heimann et al. 1975). Figure 1 illustrates a method for distinguishing convex and concave intersections. This shows that the etched fission-track channels are concave and their surface intersections are convex. In order to describe fission-track etching in apatite, it is thus necessary to determine the orientations of its fastest as well as its slowest etching faces. We take advantage of the fact that confined fission tracks provide linear concave features (except for their intersections with the host track or crack; Figure 1) at whose endpoints the slowest-etching faces develop. At the same time, their midsections present straight edges that etch at the apatite etch rate v_R perpendicular to the axis of the track, whether fast or slow. Confined tracks thus enable us to calculate v_R in all desired orientations from measurements of their width increase between two consecutive etch times.

We cut a section parallel to the ***c***-axis of a cm-sized Durango apatite, which was neither annealed nor irradiated and retained its natural complement of fossil fission tracks. We mounted it in Araldite resin, and polished the mount with 6, 3, and 1 μm diamond suspensions, finishing with a 0.04 μm silica suspension. We etched the mount for 30 s in 5.5 M HNO_3 at 21 °C (Carlson et al. 1999). The solution was mechanically stirred and its temperature continuously recorded; etching was arrested by plunging the mount consecutively in two beakers each containing ca. 250 ml of deionized water, following which the mount was allowed to dry in a curing cabinet at 35 °C. The 30 s etch is somewhat longer than usual for two reasons. First, to ensure that enough well-etched tracks are available in directions where their channels are thinnest. In general, those are the tracks sub-parallel and sub-perpendicular to the ***c***-axis. Second, to realize a range of effective etch times of the individual tracks. The effective etch time of a confined tack is the time the mount is immersed in the etchant minus that required for the etchant to bridge the distance between the host track and it. The mount was fixed on a microscope slide, to which two TEM grids were attached as reference points. The tracks were studied with a Zeiss AxioImager Z2m motorized microscope, equipped with a 100× dry objective, 2.5× post-magnification, and a Zeiss ICc3 camera. Transmitted-light digital images and coordinates of 205 horizontal confined tracks (TinT: track-in-track) were recorded with the Autoscan TrackWorks program (Gleadow et al. 2019). Plunging tracks were excluded because their shapes and dimensions cannot be contoured or measured as well as those of horizontal tracks, which are in focus over their full length at high magnification (Figure 2). The mount was then etched for another 15 s in 5.5 M HNO_3 at 21 °C, and the same tracks were imaged again. Since each track had been etched after 30 s, the effective etch time increment can be assumed to be ~15 s, although its individual total effective etch time remains unknown.

We imported the images for the 30 s and 45 s etches in the CorelDraw X6 vector graphics program (Corel Corporation) for tracing the contours, and measuring the lengths, widths, and orientations of the tracks (Figure 3). Where possible, we also measured the taper of the tracks, i.e., the cone angle between facing straight edges. Supplement 2 reports the data and Table 1 summarizes the main statistics.

Results and Discussion

Figure 4 shows the track lengths plotted against angle to the ***c***-axis. The mean and standard deviation for the 30 s etch are in reasonable agreement with fossil-track data for this, and other, etches (Jonckheere et al. 2015). The mean track lengths are somewhat lower than comparable results of an earlier experiment (Jonckheere et al. 2017). The differences are within the range of variation expected from different operators (Ketcham et al. 2015). The present lengths were measured on contours tracing the middle of the dark track outlines in transmitted light (Figure 3). This could have contributed to somewhat lower mean lengths than measurements at the microscope or on a live image. The additional 15 s etch produces a <1 μm increase of the mean and a slight decrease of the standard deviation of the track-length distribution, as also observed in earlier step-etch experiments on both fossil and induced tracks (Jonckheere et al. 2017; Tamer et al. 2019). The major and minor axis lengths of ellipses fitted to the length vs. angle to the ***c***-axis data are consistent with the model of Donelick et al. (1999) for samples etched for 20 s in 5.5 M HNO_3 at 21 °C (Table 1) This suggests that the length increase from etching and the length

This is the peer-reviewed, final accepted version for American Mineralogist, published by the Mineralogical Society of America.
The published version is subject to change. Cite as Authors (Year) Title. American Mineralogist, in press.
DOI: https://doi.org/10.2138/am-2021-7614. http://www.minsocam.org/

decrease from geological annealing possess a similar anisotropy and might in a certain sense be inverse processes. Our data are however too limited to interpret this as more than an indication, and a possible focus for future investigation.

Figure 5 plots the widths of the tracks against their ***c***-axis angles. The minimum width after 30 s is ~0.5 µm at all angles. This is considered to be the limit for selecting a track for measurement. The maximum width exhibits a strong angular dependence, peaking around ~3 µm at 60 - 75° to the ***c***-axis. The ~2.5 µm range of widths in this interval indicates a fast rate of widening. The increasing track width range up to 60 - 75° and decreasing range from 75° to 90° mirrors the angular observation frequencies of confined tracks (Barbarand et al. 2003; Ketcham 2003; Ketcham et al. 2007; Tamer et al. 2019). The rate of widening, i.e., the anisotropic apatite etch rate, is therefore thought to be an important cause of this well-known angular bias. Since the same tracks were measured after 45 s immersion, the results do not present the same flat minimum at ~0.5 µm. The width increases in 15 s are consistent with an increasing rate of widening up to 60 - 75° to the ***c***-axis before falling off again at greater angles. The limited ranges as well as the limited width increases indicate that the rates of widening are minimal parallel and perpendicular to the ***c***-axis. It is notable that, on average, the track widths increase more than the track lengths between 30 s and 45 s immersion. Figure 6 plots the cone angles θ against the track angle ϕ to the ***c***-axis (Figure 3). The cone angles, like the widths, increase up to 60 - 75°, and decrease rapidly from there to 90°. In contrast to the track widths, the cone angles show almost no increase between 30 s and 45 s immersion. The 0.3° average difference is as likely related to the measurement uncertainties as to a true increase of θ. In the latter case, the small increase between 30 and 45 s would indicate a finite but nevertheless fast rate of penetration of the etchant in the already etched track channels. Given the small difference between the 30 s and 45 s cone angles, we averaged the two measurements for the following calculations.

We calculated the rate of widening v_R from the increase $\Delta w = w_{45} - w_{30}$ from 30 s (w_{30}) to 45 s (w_{45}; Figure 3d); v_R is taken to be the apatite etch rate perpendicular to the track. We calculated the etch rates v_T of central sections of the tracks from their cone angles θ, which measure the taper of the track channels away from their intersections with the host tracks (Figure 3c). We finally calculated the rate of length increase v_L from the length difference $\Delta l = l_{45} - l_{30}$ between 30 s (l_{30}) and 45 s (l_{45}). Thus, with $\Delta t_E = 15$ s:

DOI: https://doi.org/10.2138/am-2021-7614. http://www.minsocam.org/

$$v_R\ (\mu m/min) = \frac{1}{2}\frac{\Delta w(\mu m)}{\Delta t_E(min)} \quad (2)$$

$$v_T\ (\mu m/min) = \frac{v_R\ (\mu m/min)}{tan(\theta/2)} \quad (3)$$

$$v_L\ (\mu m/min) = \frac{1}{2}\frac{\Delta l\ (\mu m)}{\Delta t_E(min)} \quad (4)$$

Figure 7 plots v_R, v_T and v_L against angle to the ***c***-axis. The apatite etch rate v_R, which replaces the former bulk etch rate v_B, shows a marked dependence on orientation, increasing from <1 µm/min parallel to ***c*** to >3 µm/min at 15 - 30°, falling off again to <1 µm/min perpendicular to ***c*** (Figure 7a). In contrast, neither the track etch rate v_T nor the length increase of confined tracks v_L exhibit a clear angular dependence. Most tracks are, in the conventional sense, fully etched, i.e., past the stage where the track etch rate applies (Laslett et al. 1984), since v_L is on average ~50 times less than v_T (Figure 7b and c). However, v_L differs from the apatite etch rate v_R as well; $v_L > v_R$ at small (≲5°) and high (≳65°) angles to ***c***, whereas $v_L < v_R$ in the intervening interval. The latter ($v_L < v_R$) implies that the confined tracks length increase at a lower rate than the apatite etch rate. This apparent paradox is nevertheless consistent with the proposed etch model (Jonckheere et al. 2019). The endpoints of the track channels are concave and, according to the model, bounded by the slowest-etching planes, i.e., the prism and basal planes, with $v_R \approx 0.5$ µm/min (Figure 7a). This implies that the rate of lengthening of confined tracks at all angles to the ***c***-axis would be ≲0.7 µm/min. With few exceptions this corresponds to the lowest rate of increase of the confined track lengths (Figure 7c). Thus a fraction of the confined tracks increases in length between 30 s and 45 s immersion at the intrinsic apatite etch rate. The fact that most tracks increase in length from 30 to 45 s at a rate that is up to four times higher implies that it is, in those cases, damage-assisted. This lends strong support to the concept of discontinuous tracks (Paul and Fitzgerald 1992; Li et al. 2011, 2012) consisting towards their ends of faster and slower-etching segments, or "unetchable" gaps (Green et al. 1986) of ≳0.2 µm that etch at the intrinsic apatite etch rate. The high v_T values, in contrast, point to a continuous midsection. These results confirm that tracks are not etched to their full potential lengths after 30 s, or even longer, in 5.5 M HNO_3 at 21 °C (Jonckheere et al. 2017; Tamer et al. 2019).

A discontinuous structure explains the otherwise unaccountable differences between tracks whose individual lengths increase between ~0.5 and ~3 µm/min. The differences are not due to measurement errors, since track lengths are easier to measure than widths (Figures 7a and c).

There is nevertheless a contributing factor: all length increments correspond to the same 15 s etch time increment, however not between the same initial and final effective etch times. This is because each track begins to etch at a different time after the sample is immersed in the etchant, depending on the time needed for the host tracks to widen and capture the confined track. This lag time is reflected in the range of track widths (~0.5 - ~3 μm; Figure 5) at 60 - 75° to the ***c***-axis, indicating that after 30 s immersion, the thickest confined tracks are etched ~5 times longer than the thinnest. We calculated the effective etch times (t_{E30} *and* t_{E45}) of individual tracks from their widths after 30 s immersion (w_{30}):

$$t_{E30}(s) = 60 \frac{w_{30}\ (\mu m)}{v_R\ (\mu m/min)} \quad (5)$$

$$t_{E45}(s) = t_{E30}(s) + 15\ s \quad (6)$$

Figure 8a shows the effective-etch-time distribution after 30 s immersion in 5.5 M HNO_3 at 21 °C. The few results for which $t_{E30} > 30$ s are a consequence of the limited precision of the width measurements and v_R calculations. Even allowing for this lack of precision, it is clear that, during the first 30 s step, different confined tracks have been etched for different durations, ranging from as short as ~5 s to almost the full immersion time of ~30 s. Figure 8b plots the length of each confined track against its effective etch times after 30 s and 45 s immersion. A regression line fitted to the data has a slope of 2.0(0.2) μm/min. This represents the rate of increase of the mean confined track length with effective etch time, averaged over all tracks, all orientations to the ***c***-axis, and the entire effective-etch time range up to 45 s. A quadratic fit indicates that the rate of length increase drops from 3.8(1.4) μm/min at 5 s to 1.1(0.4) μm/min at 45 s etching. Figure 8c plots the length increments against the effective etch time t_E after 30 s immersion. On average, tracks with shorter effective etch times increase more in length after a further 15 s immersion than tracks with longer effective etch times. The length increments of tracks etched less than ~10 s tend to lie above the overall trend. This is thought to correspond to the t_E interval where v_T transitions to v_L. However, most increments in the 30 s t_E interval lie above the value corresponding to the apatite etch rate v_R. In this sense, the tracks cannot be considered as fully etched either.

The measured apatite etch rates v_R enable calculating the shapes and dimensions of etched fission tracks using the track etch model based on the theories of crystal growth and dissolution proposed earlier (Jonckheere et al. 2019). Figure 9 is a polar plot of v_R, obtained by mirroring the v_R data

This is the peer-reviewed, final accepted version for American Mineralogist, published by the Mineralogical Society of America.
The published version is subject to change. Cite as Authors (Year) Title. American Mineralogist, in press.
DOI: https://doi.org/10.2138/am-2021-7614. http://www.minsocam.org/

between 0° and 90° to the ***c***-axis (Figure 7a) about the ***c***-axis and an axis perpendicular to it. This is not a violation of the apatite symmetry, because we measured horizontal confined tracks, i.e., all etch rates lie in the prism plane. Their mirror images obtained by rotating 180° (3 × 60°) about the ***c***-axis lie in the same plane. Mirroring about an axis perpendicular to ***c*** is consistent with the mirror plane of apatite. At present, we have no data on the variation of v_R with orientation in the apatite basal plane. Given the six-fold axis perpendicular to this plane and the constant thickness of the etched-track channels in all orientations (cf. Figure 4.7 of Fleischer et al. 1975), we can for now disregard the variation of v_R about the ***c***-axis, and assume that all apatite prism faces etch at a rate of ~0.5 µm/min (Figure 7a). These low rates lend the etched tracks their characteristic knife-blade appearance.

Figure 10 shows a sample of etched-track shapes calculated with the etch rates in Figure 9. At this stage, the calculation was done by graphical construction rather than by actual numerical methods (Jonckheere et al. 2019). The calculated examples are of 5.0 µm semi-tracks (surface tracks) intersecting apatite faces at 0°, 30°, 60° and 90° to the ***c***-axis, etched for 20 s in 5.5 M HNO_3 at 21 °C (Carlson et al. 1999). The calculation uses the v_R values from Figure 9, but ignores second-order effects due to the finite values of v_T and v_L, which are not well enough constrained to be included in the calculation. The construction therefore assumes that the latent tracks etch to their endpoints in a negligible time ($v_T \rightarrow \infty$) after which the resulting channel grows at the etch rate of undamaged apatite, i.e., residual damage that increases v_L above the intrinsic apatite etch rate v_R is not considered ($v_L \rightarrow 0$).

Our etch model explains the etched-track profiles in apatite reasonably well. Tracks in a basal face exhibit the familiar dual form consisting of an etch pyramid of constant size and an etch channel connected to its apex, whose width varies with the dip of the track (Figure 10p-t; cf. Figure 10c of Jonckheere et al. 2019). Etch pits are rare in other faces because their development cannot compete with that of the channel and surface etching. An etch pit nevertheless does form at tracks at small angles to ***c*** (Figure 10c, i, o). Those in the prism face are well documented (cf. Figure 10f of Jonckheere et al. 2019,). Some tracks sport a vestigial etch pit (Figure 10g, n) resembling a collar attached to the track opening in microscope images (cf. Figure 10i of Jonckheere et al. 2019). The shape of the track channel away from its surface intersection is not influenced by the orientation of the surface but determined by that of the track relative to the apatite ***c***-axis alone (e.g., Figure 10b, h, n, t).

The openings of the etch channels in the prism face range from ~1.8 to ~2.2 μm (Figure 10a-e). This agrees with published mean Dpar-values for 20 s etching in 5.5 M HNO_3 at 21 °C (~1.5 - 2.0 μm for Durango apatite; Ketcham et al. 2015). The proposed etch model thus accounts for the fact that Dpar is not constant but varies by ~20% (Jonckheere et al. 2020). Most etch pyramids in the basal face are a constant size due to the fact that they are much larger than the channel width (Figure 10p-t), although somewhat elongated forms develop at low dip angles. The sizes of channel openings in the intermediate faces range from <0.7 to >3 μm in the calculated examples (Figures 10f-j and 10k-o). This range agrees with that measured in an apatite section at 30° to ***c*** (Jonckheere et al. 2020). The small channel openings form at tracks at low angles to the ***c***-axis (Figure 10f, l). The slow-etching prism faces enclosing the track on all sides prevent the development of the otherwise characteristic knife-blade shape, which gives rise to the elongated surface intersections. Jonckheere et al. (2020) interpreted the small track openings in these faces as the result of surface etching. It is a contributing factor but it does not explain most track openings smaller than those in a prism face.

The surface etch rate v_S, i.e., the apatite etch rate v_R perpendicular to the polished surface, varies by a factor of ~5 as a function of orientation (Figure 10). Basal and prism faces are lowered <0.2 μm after a 20 s etch in 5.5 M HNO_3 at 21 °C. Fast-etching faces are lowered >1 μm, adding ≳10% to their track densities. However, because $v_S \gg v_L$, about an equal number is overtaken by the surface, and lost. This stands in contrast to the earlier etch model where a track, once etched, is never lost, and the surface track densities increase without limit (Tagami and O'Sullivan 2005). The fact that $v_S \gg v_L$ in fast-etching faces also causes individual tracks to become shorter (e.g., Figure 10k-o). In first approximation, the combined loss and addition of tracks due to surface etching has the overall effect that the track densities are constant and the track size distributions (etchable and projected length, and depth; Jonckheere and Van den haute 1998) are independent of etch time. The original population of surface tracks is however gradually replaced by exhumed tracks etched for a shorter time, a fraction of which will be too indistinct to be counted or measured (Jonckheere and Van den haute 1999). Factors that cannot be quantified, e.g., the length increase at a variable rate v_L above the apatite etch rate v_R, and the fact that the value of v_L may change as the faces terminating the track become exposed at the surface, complicate this first-order picture. However, it is, in our opinion, not fruitful to overvalue such second-order effects. The observation conditions and subjective track identification criteria are no doubt much more important than the subtler details of track revelation.

IMPLICATIONS

This paper presents a quantitative description of fission-track etching that explains the distinctive geometries and the dimensions of tracks in different apatite faces. The present model is for apatite etched in 5.5 M HNO_3 at 21 °C. It must be recalibrated for other etching conditions and adapted for other minerals. Its significance lies in the fact that it replaces a questionable earlier model that had remained unchallenged for fifty years. Although it predicted neither the shapes nor the dimensions of tracks in apatite, it had major practical implications, such as that track counting efficiencies are determined by the surface etch rate, and only prism faces with counting efficiencies close to ~1 are suitable for dating. These claims, based on dubious premises, can no longer be upheld in the face of empirical evidence that track counting efficiencies are at least as much a matter of the observation conditions and track identification criteria as of etch rates, well below ~1 for prism faces and other apatite faces, and dependent on the track length distribution (Jonckheere and Van den haute 1996, 2002; Jonckheere 2003; Enkelmann et al. 2005; Jonckheere et al. 2015). Our model offers a basis for reassessing the efficiencies of fission-track counts and for reinvestigating the factors that control them.

Our data show that apatite etching is anisotropic with a minimum etch rate of ~0.5 μm/min parallel and perpendicular to the ***c***-axis and a maximum of >3 μm/min between 15 and 30° to ***c*** (5.5 M HNO_3 at 21 °C). The average track etch rate v_T is of the order of 75 μm/min, more than 35 times the average apatite etch rate v_R. After a single etch step, individual confined tracks are etched between ~5 s and nearly the full immersion time in the etchant. Their mean length increases with etch time up to at least 45 s at a decreasing rate v_L that is neither the track etch rate v_T nor the apatite etch rate v_R. Measurements of the track widths and the empirical dependence of the mean track length on etch time permit, to a certain extent, to correct for sampling-related factors. There nevertheless remains a considerable irreducible residual scatter of the confined track lengths. The erratic length increments between 30 and 45 s etching indicate that this is due to track-to-track differences related to their intermittent structure (Paul and Fitzgerald 1992; Li et al. 2011, 2012; Jonckheere et al. 2017). In our opinion, little is therefore to be gained by adjusting existing etching protocols in an attempt to reveal the "true" lengths of confined tracks (Tamer et al. 2019). On the other hand, step etching and track width measurements serve to eliminate some of the sampling- and measurement-related veil, and to access more fundamental properties of the track structure. In our fossil track data, it reflects the superposition of the inseparable effects of track formation and annealing. It will therefore be interesting to extend our experiments to unannealed and partially annealed induced tracks. Closer access to measurable properties of track structure resulting from geological annealing offers the prospect of increasing the resolution of apatite fission-track modeling (Nováková et al. 2020).

A discontinuous track with respect to etching can be seen as alternating faster- and slower-etching sections. Such a structure allows disproportionate length increases for small etch time increments. Our data show that some tracks lengthen at around the apatite etch rate v_R after an initial 30 s etch step. Their etch channels terminated at slow-etching sections (unetchable gaps; Green et al. 1986), which an additional 15 s step failed to pierce. It is thus improbable that many more such gaps were pierced in tracks that showed length increments of up to 3 μm. It follows that the fast-etching segments can be of the order of a micrometer long. The final etched length of a confined track thus depends on penetrating a few slow-etching segments. This in turn must depend on the apatite etch rate v_R. This then could explain the positive correlation between the initial mean confined track length and Dpar in apatites of different chemical composition (Carlson et al. 1999; Barbarand et al. 2003). If this applies to annealed samples, the apparent greater annealing resistance of high-Dpar apatites could be in part due to their high etch rates and not uniquely to their low annealing rates. If confirmed, it would have significant implications for our understanding of the annealing mechanisms.

We conclude that the approach in this work, which combines step etching of single tracks with estimates of their effective etch times, might prove useful for understanding fundamental track properties. It can be utilized to compare fossil and induced tracks, annealed and unannealed tracks, and different apatites.

Acknowledgment and funding

Research funded by the German Research Council (DFG project Jo 358/4-1). We are much indebted to R. Ketcham and A.J.W. Gleadow for their professional reviews, which greatly improved our manuscript.

This is the peer-reviewed, final accepted version for American Mineralogist, published by the Mineralogical Society of America.
The published version is subject to change. Cite as Authors (Year) Title. American Mineralogist, in press.
DOI: https://doi.org/10.2138/am-2021-7614. http://www.minsocam.org/

References cited

Barbarand, J., Hurford, T., and Carter, A. (2003) Variation in apatite fission-track length measurement: implications for thermal history modelling. Chemical Geology, 19, 77–106.

Batterman, B.W. (1957) Hillocks, pits and etch rate in Germanium crystals. Journal of Applied Physics, 28, 1236–1241.

Burton, W.K., Cabrera, N., and Frank F.C. (1951) The growth of crystals and the equilibrium structures of their faces. Philosophical Transactions of the Royal Society of London A, 243, 299–358.

Carlson, W.D., Donelick, R.A., and Ketcham, R.A. (1999) Variability of apatite fission-track annealing kinetics: I. Experimental results. American Mineralogist, 84, 1213–1223.

Chernov, A.A. (2004) Notes on interface growth kinetics 50 years after Burton, Cabrera and Frank. Journal of Crystal Growth, 264, 499–518.

Donelick, R.A., Ketcham, R.A., and Carlson, W.D. (1999) Variability of apatite fission-track annealing kinetics: II. Crystallographic orientation effects. American Mineralogist, 84, 1224–1234.

Donelick, R.A., O'Sullivan, P.B., and Ketcham, R.A. (2005) Apatite fission-track analysis. In P. Reiners, and T. Ehlers, Eds., Low-temperature thermochronology. Reviews in Mineralogy and Geochemistry, 58, 49–94.

Enkelmann, E., Jonckheere, R., and Wauschkuhn, B. (2005) Independent fission-track ages (ϕ-ages) of proposed and accepted apatite age standards and a comparison of ϕ-, Z-, ζ- and ζ_0-ages: implications for method calibration. Chemical Geology, 222, 232–248.

Fleischer, R.L., Price, P.B., and Walker, R.M. (1975) Nuclear tracks in solids. Principles and Applications. University of California Press, Berkeley; pp. 604.

Frank, F.C. (1958) On the kinematic theory of crystal growth and dissolution processes. In T.H. Doremus, B.W Roberts, and D. Turnbull, Eds., Growth and perfection of crystals, Wiley, London, U.K, 411–419.

Frank, F.C., and Ives, M.B. (1960) Orientation-dependent dissolution of Germanium. Journal of Applied Physics, 31, 1996–1999.

Gleadow, A.J.W. (1978) Anisotropic and variable track etching characteristics in natural sphenes. Nuclear Track Detection, 2, 105–111.

Gleadow, A.J.W. (1981) Fission track dating methods: what are the real alternatives? Nuclear Tracks, 5, 3–14.

Gleadow, A.J.W., Belton, D.X., Kohn, B.P., and Brown, R.W. (2002) Fission track dating of phosphate minerals and the thermochronology of apatite. In M.J. Kohn, et al., Eds., Phosphates, Geochemical, Geobiological, and Materials Importance. Reviews of Mineralogy and Geochemistry, 48, 579–630.

Gleadow, A.J.W., Kohn, B., and Seiler, C. (2019) The future of fission track thermochronology. In M.G. Malusà, and P.G. Fitzgerald, Eds., Fission-Track Thermochronology and its Application to Geology, Springer Textbooks in Earth Sciences, Geography and Environment, 77–92.

Gleadow, A.J.W., and Seiler, C. (2015) Fission-track dating and thermochronology. In J.W. Rink, and J.W. Thompson, Eds., Encyclopedia of Scientific Dating Methods, Springer Dordrecht, 285–296.

Green, P.F., Duddy, I.R., Gleadow, A.J.W., Tingate, P.R., and Laslett, G.M. (1986) Thermal annealing of fission tracks in apatite 1. A qualitative description. Chemical Geology (Isotope Geoscience

Section), 59, 237–253.

Guo, S.-L., Chen, B.-L., and Durrani, S.A. (2020) Solid-state nuclear track detectors. In Handbook of Radioactivity Analysis, 4th edition, Volume 1: Radiation Physics and Detectors, Academic Press, 307–407.

Heimann, R., Franke, W., and Lacmann, R. (1971) Dissolution forms of single crystal spheres of rutile. Journal of Crystal Growth, 13/14, 202–206.

Heimann, R., Franke, W., and Lacmann, R. (1975) The dissolution forms of single crystal spheres. IV. Dissolution of MgO. Journal of Crystal Growth, 28, 151–156.

Holmes, P.J. (1962) Practical applications of chemical etching. In P.J. Holmes, Ed., The electro-chemistry of semiconductors, Academic Press, London, 329–377.

Hurford, A.J. (2019) An historical perspective on fission-track thermochronology. In M.G. Malusà, and P.G. Fitzgerald, Eds., Fission-Track Thermochronology and its Application to Geology, Springer Textbooks in Earth Sciences, Geography and Environment, 3–23.

Irving, B.A. (1959) Shapes of etch hillocks and pits and their correlation with measured etch rates. Journal of Applied Physics, 31, 109–111.

Irving, B.A. (1962) Chemical etching of semiconductors. In P.J. Holmes, Ed., The electro-chemistry of semiconductors, Academic Press, London, 256–289.

Jaccodine, R.J. (1962) Use of modified free energy theorems to predict equilibrium growing and etching shapes. Journal of Applied Physics, 33, 2643–2647.

Jonckheere, R. (2003) On the densities of etchable fission tracks in a mineral and co-irradiated external detector with reference to fission-track dating of minerals. Chemical Geology, 200, 41–58.

Jonckheere, R., Aslanian, C., Wauschkuhn, B., and Ratschbacher, L. (2020) Some geometrical properties of fission-track-surface intersections in apatite. American Mineralogist, in press.

Jonckheere, R., Tamer, M.T., Wauschkuhn, B., Wauschkuhn, F., and Ratschbacher, L. (2017) Single-track length measurements of step-etched fission tracks in Durango apatite: "Vorsprung durch Technik". American Mineralogist, 102, 987–996.

Jonckheere, R., and Van den haute, P. (1996) Observations on the geometry of etched fission tracks in apatite: implications for models of track revelation. American Mineralogist, 81, 1476–1493.

Jonckheere, R., and Van den haute, P. (1998) On the frequency distributions per unit area of the dimensions of fission tracks revealed in an internal and external mineral surface and in the surface of an external detector. Radiation Measurements, 29, 135–143.

Jonckheere, R., and Van den haute, P. (1999) On the frequency distributions per unit area of the projected and etchable lengths of surface-intersecting fission tracks: Influences of track revelation, observation and measurement. Radiation Measurements, 30, 155–179.

Jonckheere, R., and Van den haute, P. (2002) On the efficiency of fission-track counts in an internal and external apatite surface and in a muscovite external detector. Radiation Measurements, 35, 29–40.

Jonckheere, R., Van den haute, P., and Ratschbacher, L. (2015) Standardless fission-track dating of the Durango apatite age standard. Chemical Geology, 417, 44–57.

Jonckheere, R., Wauschkuhn, B., and Ratschbacher, L. (2019) On growth and form of etched fission tracks in apatite: A kinetic approach. American Mineralogist, 104, 569–579.

Ketcham, R.A. (2003) Observations on the relationship between crystallographic orientation and biasing in apatite fission-track measurements. American Mineralogist, 88, 817–829.

Ketcham, R.A., Carter, A.C., Donelick, R.A., Barbarand, J., and Hurford, A.J. (2007) Improved measurement of fission-track annealing in apatite using ***c***-axis projection. American Mineralogist, 92, 789–798.

Ketcham, R.A., Carter, A., and Hurford, A.J. (2015) Inter-laboratory comparison of fission track confined length and etch figure measurements in apatite. American Mineralogist, 100, 1452–1468.

Kohn, B., Chung, L., and Gleadow, A., (2019) Fission-track analysis: Field collection, sample preparation and data acquisition. In M.G. Malusà, and P.G. Fitzgerald, Eds., Fission-Track Thermochronology and its Application to Geology, Springer Textbooks in Earth Sciences, Geography and Environment, 25–48.

Laslett, G.M., Gleadow, A.J.W., and Duddy, I. (1984) The relationship between fission track length and track density in apatite. Nuclear Tracks, 9, 29–38.

Li, W., Kluth, P., Schauries, D., Rodriguez, M.D., Lang, M., Zhang, F., Zdorovets, M., Trautmann, C., and Ewing, R.C. (2014) Effect of orientation on ion track formation in apatite and zircon. American Mineralogist, 99, 1127–1132.

Li, W., Lang, M., Gleadow, A.J.W., Zdorovets, M.V., and Ewing, R.C. (2012) Thermal annealing of unetched fission tracks in apatite. Earth and Planetary Science Letters, 321-322, 121–127.

Li, W., Wang, L., Lang, M., Trautmann, C., and Ewing, R.C. (2011) Thermal annealing mechanisms of latent fission tracks: Apatite *vs*. zircon. Earth and Planetary Science Letters, 302, 227–235.

Nováková, L., Jonckheere, R., Wauschkuhn, B., and Ratschbacher, L. (2020) Thermal history modelling of the western margin of the Bohemian Massif using high-resolution apatite fission-track thermochronology. Abstracts of the EGU General Assembly, May 4-7, 2020. Tectonics and Structural Geology Session (TS2.3).

Paul, T.A., and Fitzgerald, P.G. (1992) Transmission electron microscopic investigation of fission tracks in fluorapatite. American Mineralogist, 77, 336–344.

Price, P.B., and Fleischer, R.M. (1971) Identification of energetic heavy nuclei with solid dielectric track detectors: Applications to astrophysical and planetary studies. Annual Review of Nuclear Science, 21, 95–334.

Price, P.B., and Walker, R.M. (1962) Chemical etching of charged-particle tracks in solids. Journal of Applied Physics, 33, 3407–3412.

Rakovan, J. (2002) Growth and Surface Properties of Apatite. In M.J. Kohn, et al., Eds., Phosphates, Geochemical, Geobiological, and Materials Importance. Reviews of Mineralogy and Geochemistry, 48, 51–86.

Tagami, T., and O'Sullivan, P.B. (2005) Fundamentals of fission-track thermochronology. Reviews in Mineralogy and Geochemistry, 58, 19–47.

Tamer, M.T., Chung, L., Ketcham, R.A., and Gleadow, A.J.W. (2019) Analyst and etching protocol effects on the reproducibility of apatite confined fission-track length measurement, and ambient-temperature annealing at decadal timescales. American Mineralogist, 104, 1421–1435.

Woensdregt, C.F. (1993) Hartman-Perdok theory: Influence of crystal structure and crystalline interface on crystal growth. Faraday Discussions, 95, 97–107.

Woodruff, D.P. (2015) How does your crystal grow? A commentary on Burton, Cabrera and Frank (1951) 'The growth of crystals and the equilibrium structure of their surfaces'. Philosophical transactions of the Royal Society A, 373, 1–11.

DOI: https://doi.org/10.2138/am-2021-7614. http://www.minsocam.org/

FIGURE CAPTIONS

Figure 1. Convex and concave intersections of faces bounding a fission track and the detector surface in a 2D plane section. If a circle tangent to intersecting faces lies outside the apatite (in the track channel) their intersection is concave (black); if the circle lies inside the apatite, then the intersection is convex (white). Thus the faces bounding the channel of a surface track have concave intersections with each other, but each of them has a convex intersection with the surface. The 3D track-surface intersection is thus convex-concave (Jonckheere et al. 2019, in particular Figure 6); the same applies to track-track intersections and leads to additional facets at those intersections.

Figure 2. Horizontal confined fossil tracks in various orientations in an apatite prism face, from nearly parallel (a) to almost perpendicular to the ***c***-axis (j). The track on the left in each panel was observed after 30 s immersion in 5.5 M HNO_3 at 21 °C, that on the right after 45 s. There is, in most cases, a significant increase of the track widths from 30 s to 45 s, and an, in comparison, moderate increase of their lengths (Supplement 2). In particular, after 45 s, the tracks are terminated by edges parallel to the slow-etching basal and prism faces, whose relative extent varies with orientation (cf. Figure 11 of Jonckheere et al. 2019). Tracks with orientations close to the etch-rate minima parallel and perpendicular to the ***c***-axis acquire a funnel shape due to the growth of fast-etching faces at their intersections with the host track (b and j; cf. Figure 12 of Jonckheere et al. 2019). Microscope images taken in transmitted light using 100× objective and 2.5× post-magnification.

Figure 3. Transmitted-light microscope images of a confined fossil fission track in Durango apatite after 30 s (a) and 45 s (b) immersion in 5.5 M HNO_3 at 21 °C; dashed white lines are the digitized contours. (c) Superimposed contours (white: 30 s; grey: 45 s) with the sought etch rates; v_T: track etch rate; v_R: apatite etch rate perpendicular to the track; v_L: rate of length increase; ϕ: angle between the track and the apatite ***c***-axis; θ: cone angle of the track. (d) Superimposed track contours showing measurements of the track length ($\Delta l = l_{45} - l_{30}$) and width increment ($\Delta w = w_{45} - w_{30}$). Both the width and cone angle measurements require facing straight edges at the etched track, which are most limited after 45 s etching (A-B and C-D). These sections should be affected neither by the development of slow-etching basal and prism faces, nor by rounding at the track ends. Deviations from the etch figure due to the influence of an off-center host track must be avoided.

Figure 4. Measured lengths of the same confined fission tracks after 30 s (white) and 45 s (grey) immersion in 5.5 M HNO_3 at 21 °C, plotted against angle to the ***c***-axis. The solid lines are ellipses

This is the peer-reviewed, final accepted version for American Mineralogist, published by the Mineralogical Society of America.
The published version is subject to change. Cite as Authors (Year) Title. American Mineralogist, in press.
DOI: https://doi.org/10.2138/am-2021-7614. http://www.minsocam.org/

fitted without constraints; the dashed lines are ellipses fitted with the constraint that l_C = 1.632 l_A - 10.879 (l_C = long axis parallel to the apatite ***c***-axis; l_A = short axis perpendicular to ***c***; Donelick et al. 1999).

Figure 5. Measured widths of the same confined fission tracks after 30 s (white) and 45 s (grey) immersion in 5.5 M HNO_3 at 21 °C, plotted against the angle between the track axis and the apatite ***c***-axis (cf. Figure 3d).

Figure 6. Measured cone angles of confined fission tracks after 30 s (white) and 45 s (grey) immersion in 5.5 M HNO_3 at 21 °C, plotted against the angle between the track axis and the apatite ***c***-axis (cf. Figure 3c).

Figure 7. Calculated etch rates plotted against angle to the apatite ***c***-axis (5.5 M HNO_3 at 21 °C). (a) The apatite etch rate v_R ; the solid line is a modified lognormal fit with no physical meaning; the dashed line indicates the mean rate of track length increase v_L, for comparison. (b) Track etch rate v_T of the track midsection, calculated from the cone angle of the etch channels (Figure 3c). (c) The rate of length increase of confined tracks v_L; the solid line represents the average; the dashed line indicates the theoretical rate calculated assuming that the increase of the confined track length is controlled by the etch rates v_R of the slow etching basal and prism faces of apatite.

Figure 8. Effective etch time. (a) Frequency distribution of the calculated effective etch times of confined tracks after immersion in 5.5 M HNO_3 at 21 °C for 30 s (solid) and 45 s (dashed). (b) Confined track lengths plotted against their effective etch times after immersion for 30 s and 45 s in the etchant; the solid line is a linear fit, the dashed line is a quadratic fit to the combined 30 s and 45 s data. (c) Length increments plotted against effective etch time after immersion for 30 s; the solid line is a linear fit; the dotted line is the maximum length increment due to the apatite etch rates.

Figure 9. Polar plot of the variation of the apatite etch rate v_R with orientation in a prism plane based on the data in Figure 7a, assuming mirror symmetry about axes parallel and perpendicular to the apatite ***c***-axis.

Figure 10. Sample of calculated geometries and dimensions of fission tracks intersecting apatite surfaces at 0°, 30°, 60° and 90° to the ***c***-axis; the latent tracks are 7.5 μm long and plunge 30°, 60°, 90°, 120° and 150° relative to the etched surface; the calculations are for tracks etched for 20 s in 5.5 M HNO_3 at 21 °C.

TABLES

Table 1. Statistics of confined fission tracks in Durango apatite etched for 30 s and 45 s in 5.5 M HNO_3 at 21 °C; t_E: immersion time in the etchant; N_C: number of confined tracks; l_M: mean track length; l_P: mean ***c***-axis projected length (Ketcham et al. 1999); $l_{C,U}$ and $l_{A,U}$: long and short axes of unconstrained ellipse; $l_{C,D}$ and $l_{A,D}$: long and short axes of constrained ellipse; w_M: mean track width; θ_M: mean cone angle; S.D.: standard deviation; v_R: apatite etch rate; v_T: track etch rate; v_L: rate of length increase. The values in brackets are 1σ errors.

Variable	**First etch**	**Second etch**	**Increment**
t_E [s]	30	45	15
N_C	205	205	-
l_M [µm]	14.18(0.07)	14.85(0.07)	0.67
S.D.(l_M) [µm]	0.97	0.95	-0.02
l_P [µm]	14.88(0.05)	15.40(0.05)	0.52
S.D.(l_P) [µm]	0.68	0.67	-0.01
$l_{C,U}$ [µm]	14.95(0.15)	15.68(0.15)	0.73
$l_{A,U}$ [µm]	13.81(0.09)	14.44(0.09)	0.63
$l_{C,D}$ [µm]	15.09(0.16)	15.55(0.15)	0.46
$l_{A,D}$ [µm]	13.75(0.09)	14.49(0.09)	0.74
w_M [µm]	1.14(0.04)	2.13(0.07)	0.99
S.D.(w_M) [µm]	0.58	0.90	0.32
θ_M [°]	3.21(0.13)	3.54(0.15)	0.33
S.D.(θ_M) [°]	1.50	1.52	0.02
v_R [µm/min]	1.98(0.06)	S.D. [µm/min]	0.85
v_T [µm/min]	73.6(2.09)	S.D. [µm/min]	24.1
v_L [µm/min]	1.33(0.04)	S.D. [µm/min]	0.61

AM 7614-R1 | Figure 1

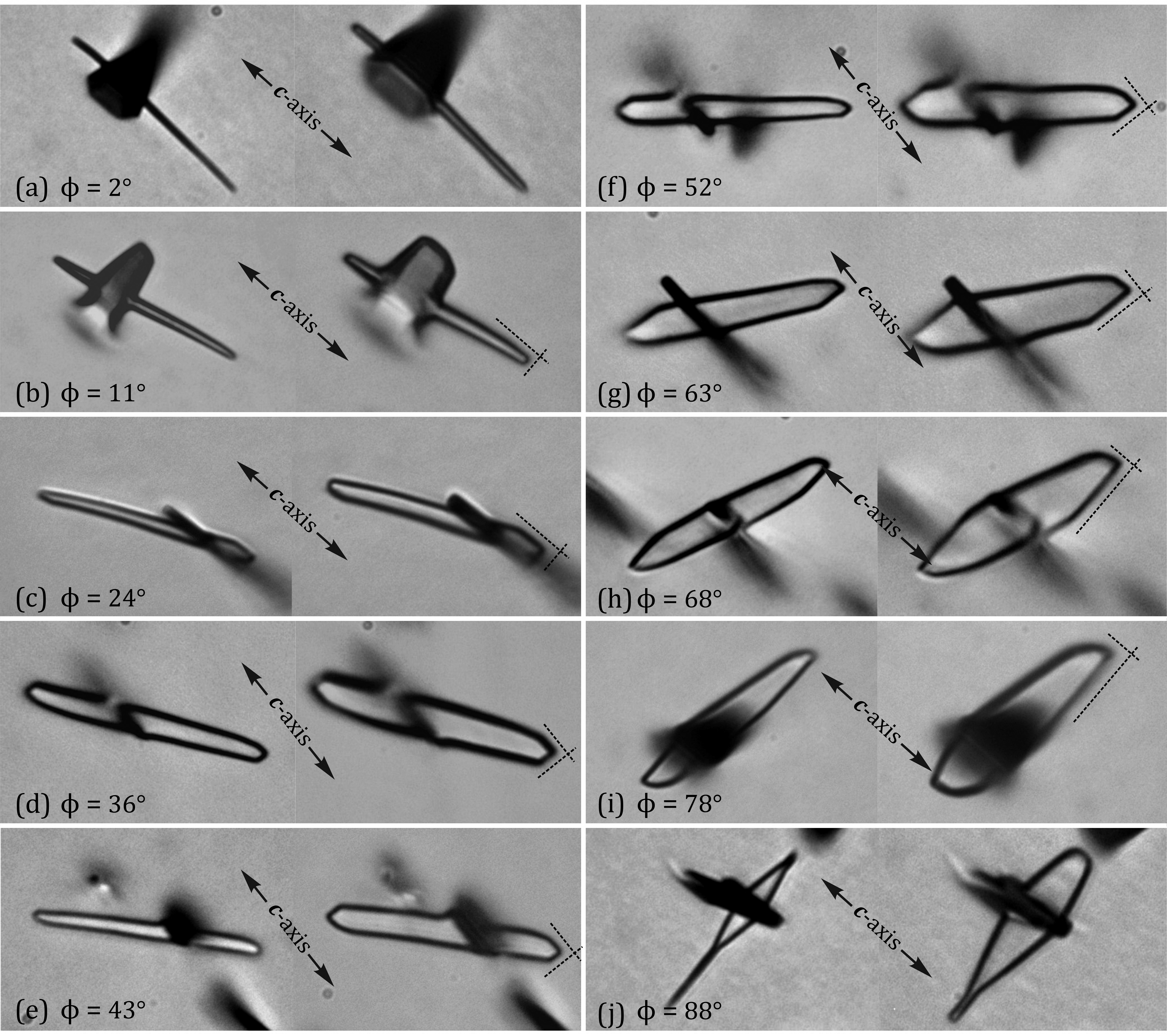
c-axis
(a) ϕ = 2°
(b) ϕ = 11°
(c) ϕ = 24°
(d) ϕ = 36°
(e) ϕ = 43°
(f) ϕ = 52°
(g) ϕ = 63°
(h) ϕ = 68°
(i) ϕ = 78°
(j) ϕ = 88°

AM 7614-R1 | Figure 3

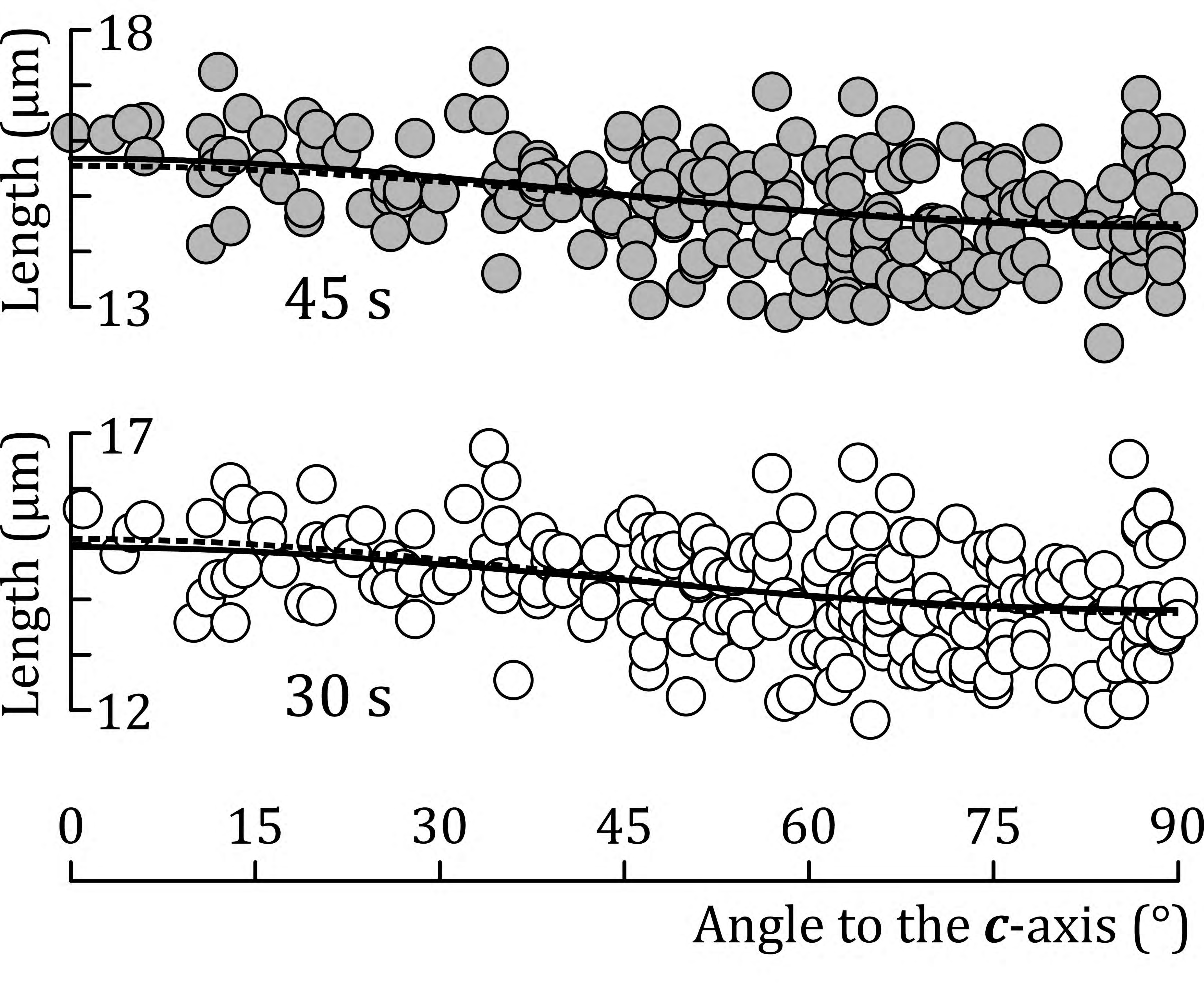

AM 7614-R1 | Figure 4

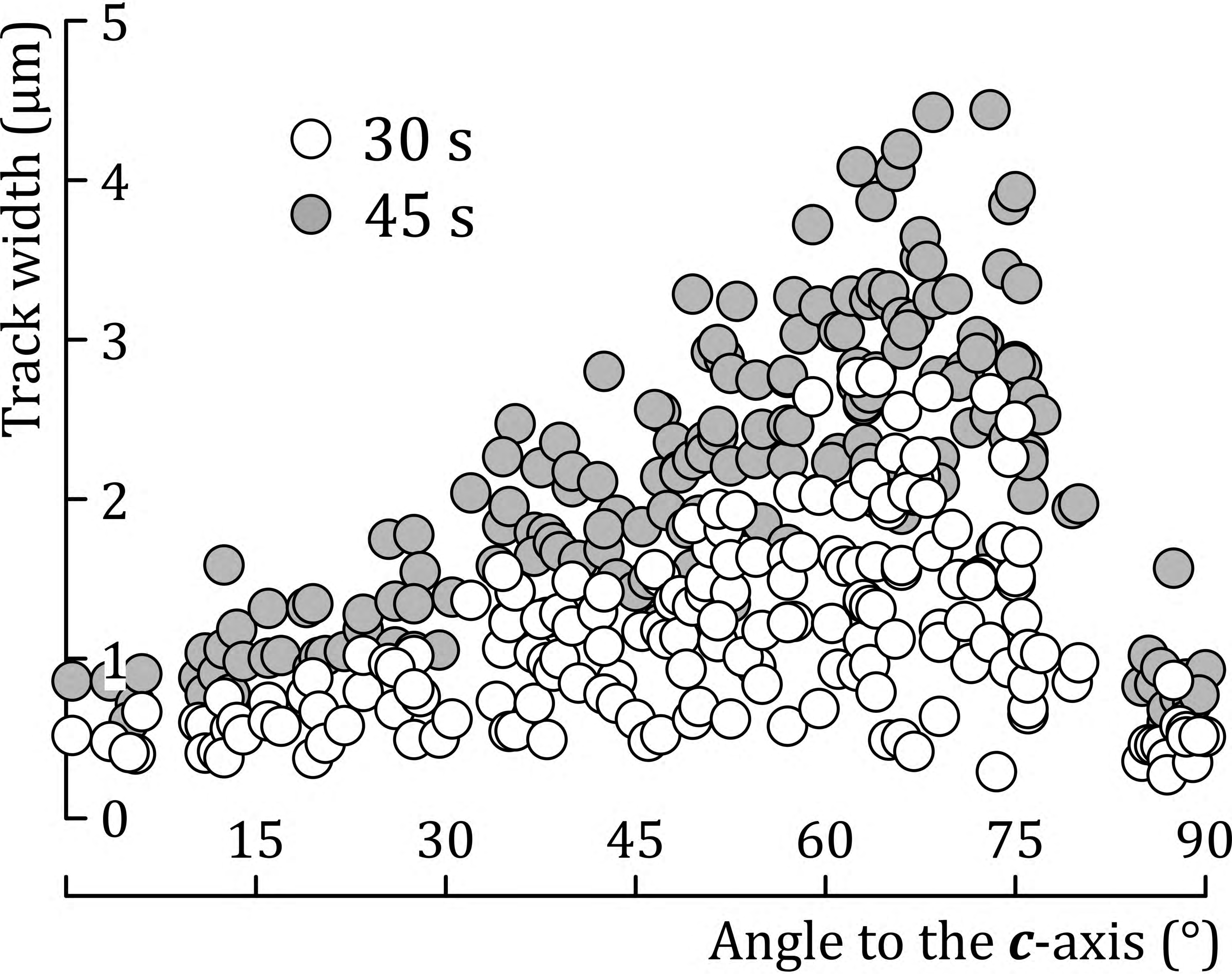

AM 7614-R1 | Figure 5

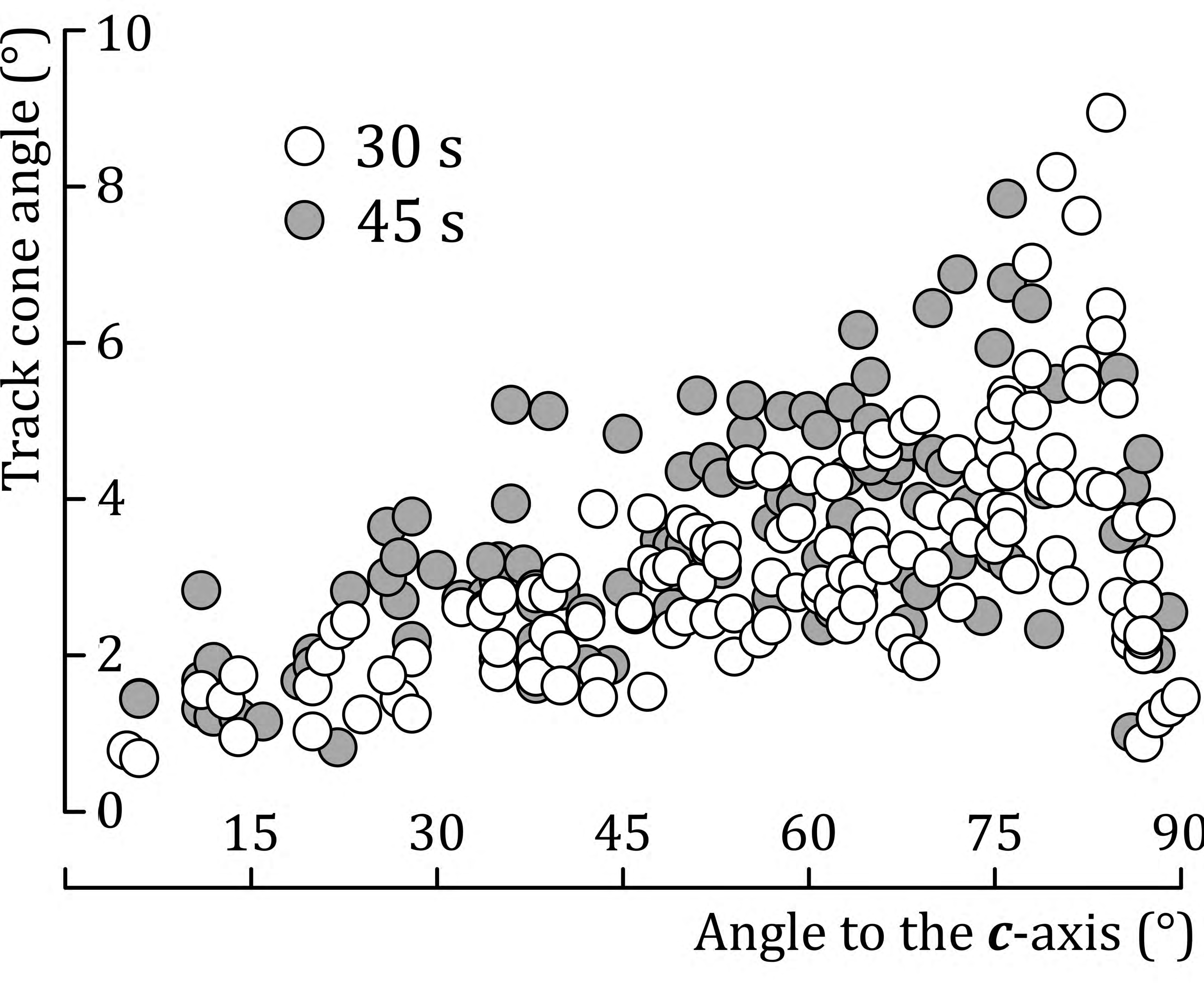

AM 7614-R1 | Figure 6

AM 7614-R1 | Figure 7

AM 7614-R1 | Figure 8

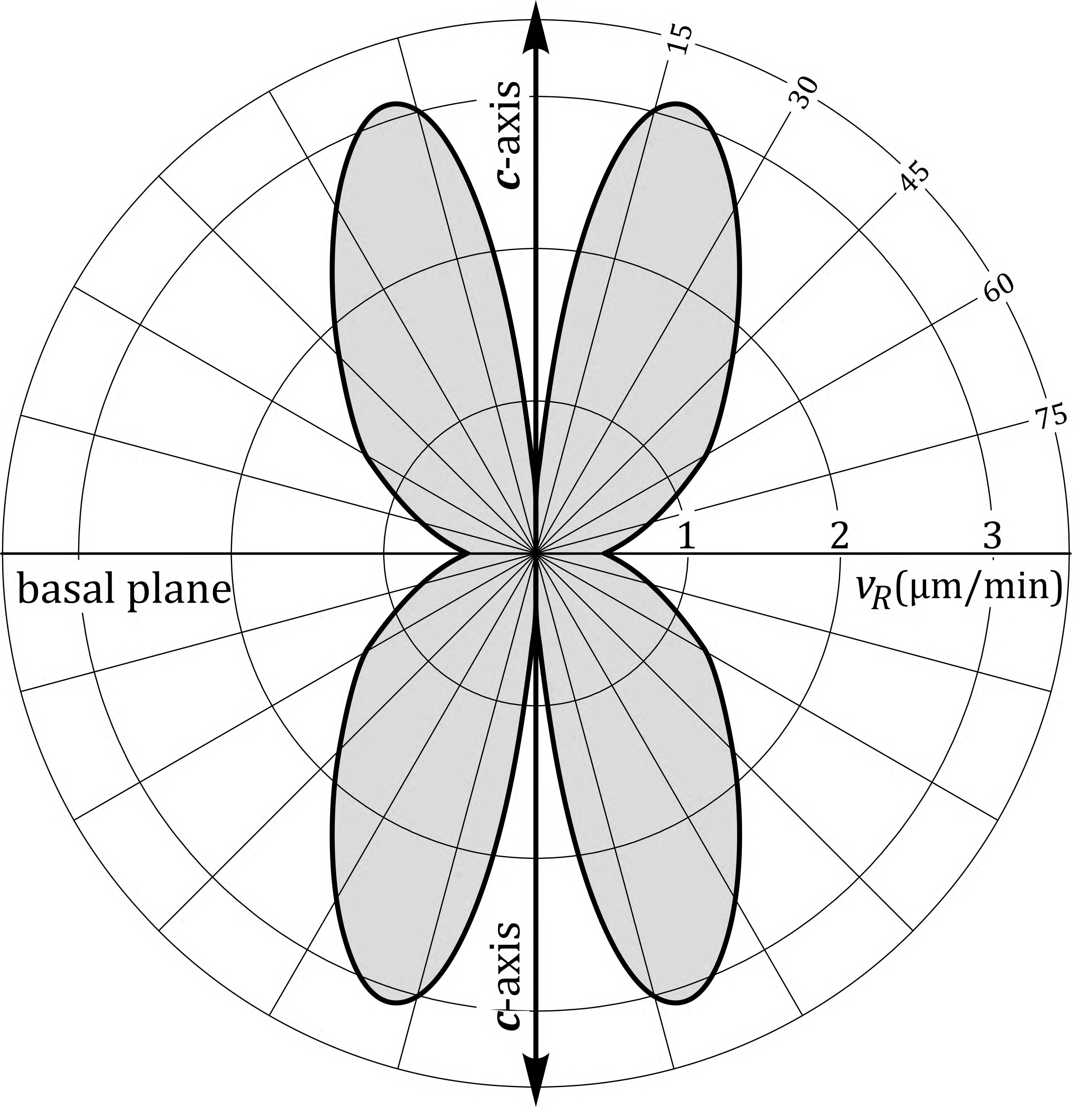

AM 7614-R1 | Figure 9

AM 7614-R1 | Figure 10